New analytical models of subthreshold surface potential and subthreshold current of fully depleted short-channel silicon-on-insulator MOSFETs with halo or pocket implantation

2014 Jpn. J. Appl. Phys. 53 064301

(http://iopscience.iop.org/1347-4065/53/6/064301)

Japanese Journal of Applied Physics **53**, 064301 (2014) **REGULAR PAPER**
http://dx.doi.org/10.7567/JJAP.53.064301

New analytical models of subthreshold surface potential and subthreshold current of fully depleted short-channel silicon-on-insulator MOSFETs with halo or pocket implantation

Han-Pang Wang

Department of Electronics Engineering, National Chiao Tung University, Hsinchu, Taiwan 300, R.O.C.
E-mail: yvonne0910@yahoo.com

Received December 26, 2013; revised February 25, 2014; accepted March 13, 2014; published online May 1, 2014

New analytical models of the subthreshold surface potential, threshold voltage and subthreshold current of fully depleted (FD) silicon on insulator MOSFETs with halo or pocket implants are presented. The subthreshold surface potential model is based on the solutions of the quasi-two-dimensional (2D) Poisson's equation, which rigorously satisfy the boundary conditions of the continuity of the potential and electric field in the lateral direction along the channel surface of halo MOS transistors. Closed-form model equations without any fitting empirical formula correctly and efficiently generate the surface potential distribution between the source and drain regions. The drain-induced barrier lowering effect of deep-submicrometer halo MOSFETs is also addressed in the present models. On the basis of the subthreshold surface potential, analytical models of the threshold voltage and subthreshold current are also developed for deep-submicrometer halo MOSFETs. The subthreshold current model is derived using the conventional drift-diffusion current theory considering the nonuniform doping profiles of a silicon film of fully-depleted silicon-on-insulator (SOI) MOS devices with halo implants. The results obtained using the model have been compared with those obtained using the device simulation software Medici to show the validity of the proposed model, and good agreement is achieved between the two. The use of the presented models can be treated as an alternative to 2D numerical analysis and used for the design of deep-submicrometer FD SOI MOSFETs with halo or pocket implants.

1. Introduction

The fully depleted silicon-on-insulator (FD SOI) MOSFETs offer superior electrical characteristics over bulk MOSFETs[1,2] such as reduced junction capacitances, increased channel mobility, suppressed short-channel effect, excellent latchup immunity, and improved subthreshold characteristics,[3,4] and therefore they have recently been attracting much attention as a potential candidate for VLSI low-voltage and -power applications.

As the channel length of MOSFETs is scaled down to the deep-submicrometer regime, several short-channel effects are observed such as the serious threshold voltage roll-off due to the charge-sharing between the drain/source and channel regions, off-state leakage current due to the sensitivity of the source/channel potential barrier to the drain bias voltage or drain-induced barrier lowering (DIBL), and bulk punch-through. In order to suppress such short-channel effects and improve device performance, lateral-channel engineering utilizing halo or pocket implants[5–15] surrounding the drain and source regions of short-channel devices has been used. The improvement can be observed as a delayed onset of threshold voltage roll-off or even increased threshold voltage and a suppressed subthreshold leakage current for deep-submicrometer MOSFETs.

To correctly predict short-channel effects, solving the two-dimensional (2D) Poisson's equation for the channel potential in the channel depletion region of deep-submicrometer SOI MOSFETs is a very important step. 2D numerical device simulators such as Medici[16] can provide the most accurate solutions of the 2D Poisson's equation. However, in order to reduce time and cost of 2D numerical simulation, analytical models have been used for MOSFET device design. An analytical model of FD SOI MOSFETs has already been used by numerous authors.[17–26] Among them, several analytical models have been developed[17–19] on the basis of the concept of a 2D charge-sharing scheme between the gate and source/drain regions to develop a threshold-voltage model of current–voltage (I–V) characteristics. However, the scheme of charge sharing is less or more arbitrary and oversimplified, and leads to an underestimated threshold voltage roll-off. In Refs. 21–23, authors utilized parabolic potential distributions for the 2D Poisson's equation and developed analytical models of drain-induced barrier lowering. A compact model based on a surface-potential-based description solves Poisson's equation explicitly in Ref. 24. However, a number of iteration steps are needed to solve Poisson's equation which on average is a factor 2 larger than that in the bulk MOSFET case, which results in a long computation time. In Ref. 18, the 2D Poisson's equation was separated into a 1D Poisson's equation and a 2D Laplace equation. In Refs. 25 and 26, full 2D analytical solutions of the 2D Poisson's equation by Green's function technique were reported. However, the analytical models mentioned above did not take into account the effect of the channel doping profile on the characteristics of FD SOI MOSFETs, such as halo or pocket implants along the channel region. Therefore, these analytical models are appropriate for a device channel with a uniform doping profile. In Ref. 27, a 2D threshold voltage model was developed for FD short-channel Si-SOI MESFETs with a nonuniform Gaussian doping profile. It expressed the function of the potential distribution in terms of the back surface potential function. However, the important parameter used to derive threshold voltage model, that is, the position of the minimum back surface potential, can only be obtained by solving complicated equations numerically. A closed-form solution of the position of the minimum back surface potential may not possible in this case. In Ref. 28, Rao et al. reported an analytical threshold voltage model of nonuniformly doped dual metal gate (DG) FD SOI MOSFETs. They developed a 2D Poisson's equation solution by separating the 2D Poisson's equation into a 1D Poisson's equation and a 2D Laplace equation. Despite the accuracy of this model, the Fourier coefficients of the electric displacement at the Si–SiO_2 interface were given in an infinite series rather than in a close (finite) form, and involved a high mathematical complexity and much difficulty to apply and understand. In Ref. 29, an analytical threshold voltage model

of SOI MOSFETs accounting for halo implants based on the three-zone Green's function solution technique was developed. Although an explicit form of the threshold voltage was derived, it involved the infinite Fourier series terms and the calculation was too complicated to be further implemented in the derivation of a *I–V* model for a circuit simulator such as SPICE. Other than the analytical threshold voltage models, a number of 2D subthreshold current models of SOI MOSFETs have been developed in studies reported in Refs. 30–32. However, without considering the effects of halo implants on the subthreshold current, they are suitable for only SOI MOSFETs with a uniform channel doping concentration.

In this paper, analytical models of the subthreshold surface potential in the silicon film, threshold voltage and subthreshold current of FD SOI MOSFETs with halo or pocket implants are proposed. The subthreshold surface potential model based on the solutions of the quasi-2D Poisson's equation accurately describes the surface potential distribution in the silicon film using simple polynomial functions and is suitable for SOI MOSFETs with halo implants or a uniformly doped profile in the silicon film. Subsequently, analytical models of the threshold voltage and subthreshold current are derived for SOI halo MOSFETs explicitly accounting for the DIBL effect and drift-diffusion current, respectively. The model results of the subthreshold surface potential distribution, threshold voltage, and subthreshold current of both deep-submicrometer and long-channel halo MOSFETs have been verified against the results of the 2D numerical simulations, and good agreement is obtained in wide ranges of structural parameters.

2. Analytical model

2.1 Subthreshold surface potential model

Figure 1 shows a schematic cross-sectional view of a halo-implanted n-MOSFET for the modeling of the subthreshold surface potential along the channel length between the source and drain regions. Heavily doped regions named the halo regions exist near the source and drain regions, whereas a lightly doped region named the channel region is located at the center of the silicon film. L is the channel length, which is the distance between the edges of the n^+-type regions of the source and drain of the halo MOSFETs. N_A and N_B are the doping concentrations in the halo and channel regions, respectively. L_1 and $(L_2 - L_1)$ are the lengths of the halo and channel regions, respectively. t_f and t_b are the thicknesses of the front gate oxide and bottom oxide, respectively. t_{si} is the thickness of the silicon film. The gate, source, and drain regions are made of n^+-type polycrystalline silicon.

Assuming that the impurity density in the halo and channel regions is uniform, and the effect of charge carriers and fixed oxide charges on the electrostatics of the channel can be neglected, the potential distribution in the silicon film can be written as

$$\frac{\partial^2 \Psi(x,y)}{\partial x^2} + \frac{\partial^2 \Psi(x,y)}{\partial y^2} = -\frac{\rho(x,y)}{\varepsilon_{si}} \qquad 0 \le x \le L, \quad 0 \le y \le t_{si}, \tag{1}$$

where $\rho(x, y)$ is the 2D charge density of the silicon film and ε_{si} is the permittivity of the silicon film. The potential profile in the vertical direction, i.e., the y dependence of $\Psi(x, y)$ can be approximated by a simple parabolic function, as discussed in Refs. 21 and 29 for the FD SOI MOSFETs and may be given as

$$\Psi(x,y) = \Psi_s(x) + c_1(x)y + c_2(x)y^2 + c_3(x)y^3, \tag{2}$$

where $\Psi_s(x)$ is the surface potential and the arbitrary coefficients $c_1(x)$, $c_2(x)$, and $c_3(x)$ are functions of x only. In the MOS devices with halo implants, since the doping distribution in the silicon film is divided into three parts as shown in Fig. 1, the potential functions in the channel and halo regions can be written as

$$\Psi_i(x,y) = \Psi_{s,i}(x) + c_{i1}(x)y + c_{i2}(x)y^2 + c_{i3}(x)y^3, \quad \begin{cases} i=1, & 0 \le x \le L_1, & 0 \le y \le t_{si} \\ i=2, & L_1 \le x \le L_2, & 0 \le y \le t_{si} \\ i=3, & L_2 \le x \le L, & 0 \le y \le t_{si} \end{cases}, \tag{3}$$

where $\Psi_i(x, y)$ and $\Psi_{s,i}(x, y)$ indicate the potential function and surface potential in the region i, respectively. From the energy band diagram in Fig. 2 of the SOI MOS structure in Fig. 1, the surface potential is $\Psi_s \equiv [E_i(0) - E_f]/(-q)$ and the band bending at the silicon surface is $\phi_s \equiv [E_i(0) - E_i(\infty)]/(-q)$, where E_f is the extrinsic Fermi level of the silicon, and $E_i(0)$ and $E_i(\infty)$ are the intrinsic Fermi levels at the surface of the silicon and in the silicon bulk, respectively. Then, we have the relation $\Psi_s(x) = \phi_s(x) - \Psi_{FP}(x)$ between $\Psi_s(x)$ and $\phi_s(x)$ at the front surface of the silicon film, where $\Psi_{FP}(x) = V_T \cdot \ln[N(x)/n_i]$, $V_T = kT/q$ is the thermal voltage, and $N(x)$ and n_i are the doping concentration in the silicon film and the intrinsic carrier concentration of silicon, respectively.

Poisson's equation is solved separately in the channel and halo regions using the following boundary conditions.

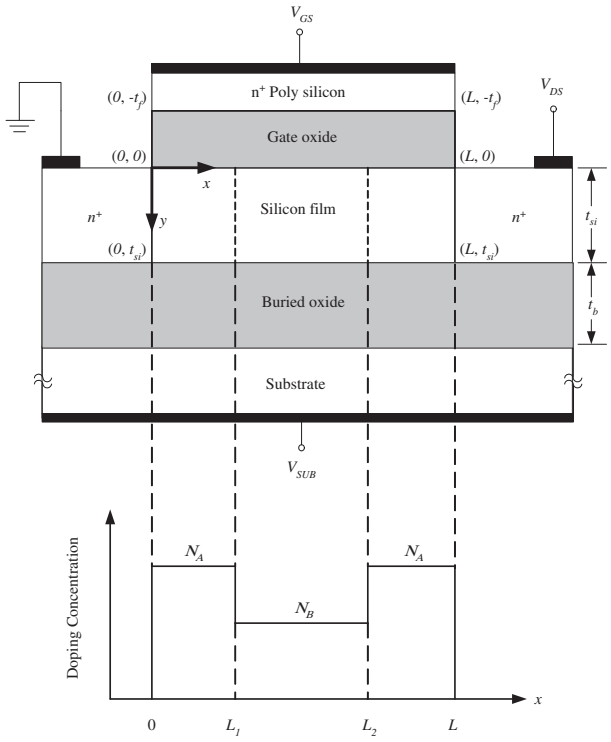

Fig. 1. Cross-sectional view of an n-channel fully-depleted SOI MOSFET. The structure has been simplified by neglecting of doping gradients in the y-direction to focus on only the average doping values of N_A and N_B.

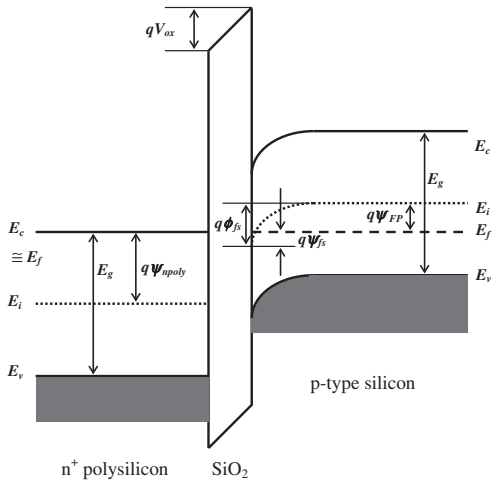

Fig. 2. Energy band diagram for $V_{GS} = 0$ V of an n-MOSFET with n$^+$-polysilicon gate and p-type silicon film. The potentials Ψ_{fs}, ϕ_{fs}, Ψ_{FP}, and Ψ_{npoly} are defined in the diagram, where qV_{ox} is the band bending at SiO_2 and E_g is the band gap of silicon.

1) The electric flux at the front gate oxide/silicon film interface is continuous for each region i and can be given as

$$\left.\frac{\partial \Psi_i(x,y)}{\partial y}\right|_{y=0} = \frac{\varepsilon_{ox}}{\varepsilon_{si}} \frac{\Psi_{fs,i}(x) - V'_{GS,i}}{t_f}, \tag{4}$$

where $\Psi_{fs,i}(x) = \Psi_{s,i}(x,0)$ is the front surface potential along the channel length in region i, ε_{ox} is the permittivity of the oxide and

$$V'_{GS,i} = V_{GS} - V_{fbf,i} - \Psi_{FP,i},$$

where V_{GS} is the gate–source bias voltage, $V_{fbf,i}$ is the front-channel flatband voltage in region i, and $\Psi_{FP,i}$ is the difference between the extrinsic Fermi level and the intrinsic Fermi level in region i and is expressed as

$$\begin{aligned} \Psi_{FP,1} &= \Psi_{FP,3} = V_T \ln(N_A/n_i), \\ \Psi_{FP,2} &= V_T \ln(N_B/n_i). \end{aligned} \tag{5}$$

2) The electric flux at the bottom oxide/silicon film interface is continuous for each region i and can be given as

$$\left.\frac{\partial \Psi_i(x,y)}{\partial y}\right|_{y=t_{si}} = \frac{\varepsilon_{ox}}{\varepsilon_{si}} \frac{V'_{SUB,i} - \Psi_{bs,i}(x)}{t_b}, \tag{6}$$

where $\Psi_{bs,i}(x) = \Psi_{s,i}(x, t_{si})$ is the back surface potential along the channel length in region i, and

$$V'_{SUB,i} = V_{SUB} - V_{fbb,i} - \Psi_{FP,i},$$

where V_{SUB} is the substrate-source bias voltage, and $V_{fbb,i}$ is the back-channel flatband voltage in region i.

3) The surface potential at the interface of the different regions is continuous:

$$\begin{aligned} \Psi_1(L_1, y) &= \Psi_2(L_1, y), \\ \Psi_2(L_2, y) &= \Psi_3(L_2, y). \end{aligned} \tag{7}$$

4) The electric flux at the interface of the different regions is continuous:

$$\begin{aligned} \left.\frac{\partial \Psi_1(x,y)}{\partial x}\right|_{x=L_1} &= \left.\frac{\partial \Psi_2(x,y)}{\partial x}\right|_{x=L_1}, \\ \left.\frac{\partial \Psi_2(x,y)}{\partial x}\right|_{x=L_2} &= \left.\frac{\partial \Psi_3(x,y)}{\partial x}\right|_{x=L_2}. \end{aligned} \tag{8}$$

5) The potential at the source end is

$$\Psi_1(0,0) = \Psi_{fs,1}(0) = V_{bi}. \tag{9}$$

6) The potential at the drain end is

$$\Psi_1(L,0) = \Psi_{fs,3}(L) = V_{bi} + V_{DS}. \tag{10}$$

Here $V_{bi} = \Psi_{npoly} \approx E_g/(2q)$ is the built-in potential across the body-source junction, and V_{DS} is the drain–source bias voltage.

The constants $c_{i1}(x)$, $c_{i2}(x)$, and $c_{i3}(x)$ in Eq. (3) can be deduced from the boundary conditions Eqs. (4)–(6) and are given as

$$\begin{aligned} c_{i1}(x) &= \frac{C_f}{\varepsilon_{si}} \cdot (\Psi_{fs,i} - V'_{GS,i}), \\ c_{i2}(x) &= \frac{1}{t_{si}^2} \cdot \left[-\left(3 + \frac{2C_f}{C_{si}}\right) \cdot \Psi_{fs,i} + \left(3 + \frac{C_b}{C_{si}}\right) \cdot \Psi_{bs,i} \right. \\ &\quad \left. - \frac{C_b}{C_{si}} \cdot V'_{SUB,i} + \frac{2C_f}{C_{si}} \cdot V'_{GS,i} \right], \\ c_{i3}(x) &= \frac{1}{t_{si}^3} \cdot \left[\left(2 + \frac{C_f}{C_{si}}\right) \cdot \Psi_{fs,i} - \left(2 + \frac{C_b}{C_{si}}\right) \cdot \Psi_{bs,i} \right. \\ &\quad \left. + \frac{C_b}{C_{si}} \cdot V'_{SUB,i} - \frac{C_f}{C_{si}} \cdot V'_{GS,i} \right], \end{aligned} \tag{11}$$

where $C_{si} = \varepsilon_{si}/t_{si}$, $C_f = \varepsilon_{ox}/t_f$, and $C_b = \varepsilon_{ox}/t_b$ are the silicon film, front gate oxide, and bottom oxide capacitances, respectively. Substituting $\Psi_i(x,y)$ from Eq. (3) into Eq. (1), and using the expressions of $c_{i1}(x)$, $c_{i2}(x)$, and $c_{i3}(x)$ in Eq. (11), the front and bottom surface potentials in region i, i.e., $\Psi_{fs,i}(x)$ and $\Psi_{bs,i}(x)$, respectively, can be expressed in terms of second-order nonhomogenous differential equations given by

$$\begin{aligned} \frac{\partial^2 \Psi_{fs,i}(x)}{\partial x^2} + A_i \Psi_{fs,i}(x) + B_i \Psi_{bs,i}(x) &= C_i, \\ \frac{\partial^2 \Psi_{bs,i}(x)}{\partial x^2} + F_i \Psi_{fs,i}(x) + G_i \Psi_{bs,i}(x) &= H_i, \end{aligned} \tag{12}$$

where the expressions of the coefficients A_i, B_i, C_i, F_i, G_i, and H_i are given in Appendix A. According to Ref. 33, the analytical solution of the above differential equations can be obtained in the following forms:

$$\begin{aligned} \Psi_{fs,i}(x) &= \Psi_{fsp,i} + a_{i1} \cdot g_1 \cdot e^{d_1 x} + a_{i2} \cdot g_1 \cdot e^{-d_1 x} \\ &\quad + a_{i3} \cdot g_2 \cdot e^{d_2 x} + a_{i4} \cdot g_2 \cdot e^{-d_2 x}, \\ \Psi_{bs,i}(x) &= \Psi_{bsp,i} + a_{i1} \cdot e^{d_1 x} + a_{i2} \cdot e^{-d_1 x} \\ &\quad + a_{i3} \cdot e^{d_2 x} + a_{i4} \cdot e^{-d_2 x}, \end{aligned} \tag{13}$$

where the particular solutions $\Psi_{fsp,i}(x)$ and $\Psi_{bsp,i}(x)$, and the constants g_1, g_2, d_1, and d_2 are given in the Appendix B. By using the boundary conditions Eqs. (7)–(10), we can obtain the expressions of the coefficients a_{i1}, a_{i2}, a_{i3}, and a_{i4} as shown in Appendix C. Finally, the surface potential distributions along the interfaces of the front-gate oxide/silicon and bottom-oxide/silicon films can be respectively obtained as

$$\begin{aligned} \Psi_{fs}(x) &= \Psi_{fs,1}(x) + \Psi_{fs,2}(x) + \Psi_{fs,3}(x), \\ \Psi_{bs}(x) &= \Psi_{bs,1}(x) + \Psi_{bs,2}(x) + \Psi_{bs,3}(x). \end{aligned} \tag{14}$$

2.2 Threshold voltage model

In SOI MOS devices with halo or pocket implants, since the doping concentrations in the channel and halo regions are different, the Fermi potential depends on the lateral location within the silicon film. Consequently, the threshold voltages

in the halo and channel regions ($V_{TH,1}$ and $V_{TH,2}$, respectively) are defined as

$$V_{TH,1} = V_{GS} \text{ at } \Psi_{fs,1}(x_{min,1}) = \Psi_{FP,1},$$
$$V_{TH,2} = V_{GS} \text{ at } \Psi_{fs,2}(x_{min,2}) = \Psi_{FP,2}, \quad (15)$$

where $x_{min,1}$ and $x_{min,2}$ are the lateral positions of the minimum surface potentials in the halo and channel regions, respectively. Then, the threshold voltage of the FD SOI MOSFET is defined by the maximum of these two voltages:

$$V_{TH} = \max\{V_{TH,1}, V_{TH,2}\}. \quad (16)$$

Equation (16) ensures the validity of the 2D analytical model for calculating a threshold voltage for which the front gate/silicon interface of the FD SOI MOS transistor is simply inverted.

Next, the positions of the minimum surface potentials $x_{min,1}$ and $x_{min,2}$ can be obtained by differentiating Eq. (3) with respect to x at $y = 0$ and solved using

$$\left.\frac{\partial \Psi(x,y)}{\partial x}\right|_{y=0} = 0. \quad (17)$$

Note that, owing to the three regions of the device shown in Fig. 1, there are three values of x_{min} in the solutions of Eq. (17). However, since the drain–source bias voltage V_{DS} is positive for an n-MOSFET, the lateral position of the minimum potential $x_{min,1}$ is always located near the source region. Therefore, only the channel and halo regions near the source side should be considered.

It may be observed that the closed form solution of the lateral position of the minimum surface potential x_{min} is not possible in this case. However, for different values of V_{GS} and V_{DS}, x_{min} may be obtained by solving Eq. (17) numerically. Consequently, it is clear that explicit expressions of both the threshold voltages $V_{TH,1}$ and $V_{TH,2}$ can be deduced from Eq. (13) by replacing V_{GS} and $\Psi_{fs,i}$ with $V_{TH,i}$ and $\Psi_{FP,i}$, respectively, where $i = 1$ or 2, and expressed as

$$V_{TH,1} = \frac{\Psi_{FP,1} - \gamma_2 \cdot V_{SUB} - \gamma_3}{\gamma_1}, \quad (18)$$

$$V_{TH,2} = \frac{\Psi_{FP,2} - \beta_2 \cdot V_{SUB} - \beta_3}{\beta_1}, \quad (19)$$

where

$$\gamma_1 = g_1\alpha_1 e^{d_1 x_{min,1}} + g_1\alpha_4 e^{-d_1 x_{min,1}} + g_2\alpha_7 e^{d_2 x_{min,1}} + g_2\alpha_{10} e^{-d_2 x_{min,1}} + \lambda_1,$$
$$\gamma_2 = g_1\alpha_2 e^{d_1 x_{min,1}} + g_1\alpha_5 e^{-d_1 x_{min,1}} + g_2\alpha_8 e^{d_2 x_{min,1}} + g_2\alpha_{11} e^{-d_2 x_{min,1}} + \lambda_2,$$
$$\gamma_3 = g_1\alpha_3 e^{d_1 x_{min,1}} + g_1\alpha_6 e^{-d_1 x_{min,1}} + g_2\alpha_9 e^{d_2 x_{min,1}} + g_2\alpha_{12} e^{-d_2 x_{min,1}} + \lambda_3,$$
$$\beta_1 = g_1\delta_1 e^{d_1 x_{min,2}} + g_1\delta_4 e^{-d_1 x_{min,2}} + g_2\delta_7 e^{d_2 x_{min,2}} + g_2\delta_{10} e^{-d_2 x_{min,2}} + \lambda_1,$$
$$\beta_2 = g_1\delta_2 e^{d_1 x_{min,2}} + g_1\delta_5 e^{-d_1 x_{min,2}} + g_2\delta_8 e^{d_2 x_{min,2}} + g_2\delta_{11} e^{-d_2 x_{min,2}} + \lambda_2,$$
$$\beta_3 = g_1\delta_3 e^{d_1 x_{min,2}} + g_1\delta_6 e^{-d_1 x_{min,2}} + g_2\delta_9 e^{d_2 x_{min,2}} + g_2\delta_{12} e^{-d_2 x_{min,2}} + \lambda_4.$$

Then, the threshold voltage of the FD SOI MOS transistor is obtained by taking the maxima of Eqs. (18) and (19).

2.3 Subthreshold current model

In the subthreshold region of SOI MOSFET operation, the depletion charge is much larger than the inversion carrier, thus the diffusion current component is expected to be dominant. However, since the potential distribution in the silicon film varies along the channel, the drift current component may contribute to the subthreshold current flow. On the basis of the drift-diffusion current theory, the electron current density in the n-MOSFET can be expressed as

$$J_n = -q\mu_n n \frac{\partial \phi_{fs}(x)}{\partial x} + qD_n \frac{\partial n(x)}{\partial x}, \quad (20)$$

where $n(x)$ is the electron density along the channel length and D_n is the electron diffusion coefficient, which can be related to the thermal voltage V_T and the electron mobility μ_n through the Einstein relation as $D_n = \mu_n \cdot V_T$. Multiplying Eq. (20) by an integrating factor of $\exp[-\phi_{fs}(x)/V_T]$, the right-hand side of the equation can be transformed into an exact derivative. With the boundary conditions in Eqs. (9) and (10), we can obtain

$$J_n = -qD_n N_A \cdot \exp\left(-\frac{V_{bi}}{V_T}\right) \cdot \frac{\left[1 - \exp\left(\frac{-V_{DS}}{V_T}\right)\right]}{\int_0^L \exp\left(-\frac{\phi_{fs}(x)}{V_T}\right) \cdot dx}. \quad (21)$$

The subthreshold current can be obtained by integrating the current density over the cross section of the conducting channel, yielding

$$I_{SUB} = J_n \cdot W \cdot d, \quad (22)$$

where W is the device channel width and d is the effective channel thickness, which can be estimated as the distance from the surface to the position where the electrostatic potential changed with V_T.[34] According to Gauss' Law, the vertical component of the electric field at the surface, V_T/d, is equal to Q_{dep}/ε_{si}, where Q_{dep} is the depletion charge. Thus, the effective channel thickness d can be obtained as

$$d = V_T \cdot \left[\frac{\varepsilon_{si}}{2qN_{AV} \cdot (\phi_{fs,inv} + V_{GT}/\theta)}\right], \quad (23)$$

where N_{AV} is the effective doping density within the channel, $\phi_{fs,inv}$ is the surface potential at the onset of strong inversion, $\phi_{fs,inv} = 2\Psi_{FP}$, $V_{GT} = V_{GS} - V_{TH}$, and θ is the subthreshold ideality factor reflecting the gate voltage division between the insulator capacitance and the silicon depletion layer capacitance. Note that the effective channel thickness given in Eq. (23) is only valid for $-\phi_{fs,inv} < V_{GT}/\theta < 0$, i.e., the weak inversion and depletion operations. The effective doping profile within the channel can be approximated by the effective channel concentration N_{AV} developed on the basis of the voltage-doping transformation:[35]

$$N_{AV} = N_B + 2 \cdot (N_A - N_B) \cdot (L_1/L) - (2\varepsilon_{si}/q) \cdot (V_{DS} + v \cdot V_{bi})/L^2, \quad (24)$$

where v is a fitting parameter. Substituting Eqs. (21)–(24) into Eq. (22), the subthreshold current can be obtained.

3. Results

In order to verify the analytical models of surface potential distribution and subthreshold current, the 2D numerical device simulator Medici is used with the halo n-MOSFET

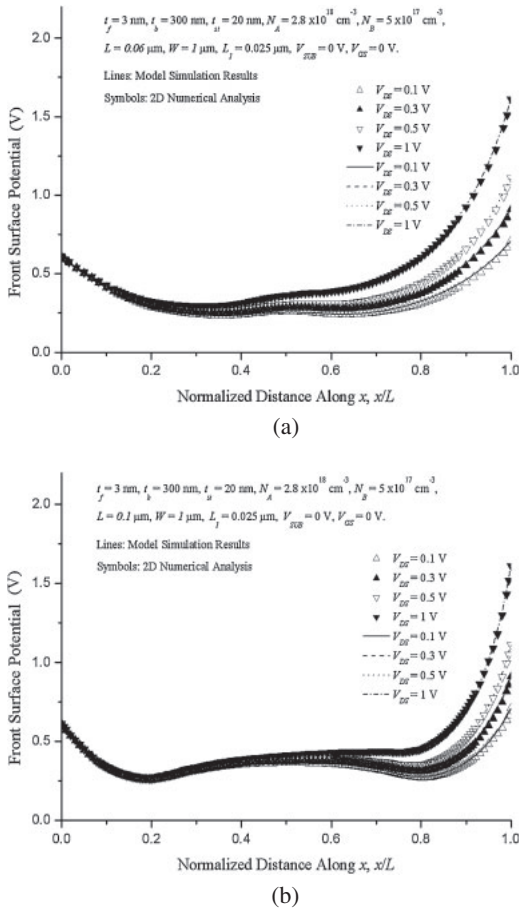

Fig. 3. Front surface potential $\Psi_{fs}(x)$ as a function of the normalized position (x/L) along the channel length for FD halo-implanted SOI MOSFETs with different gate lengths and drain bias voltages. (a) $L = 0.06\,\mu$m and (b) $L = 0.1\,\mu$m.

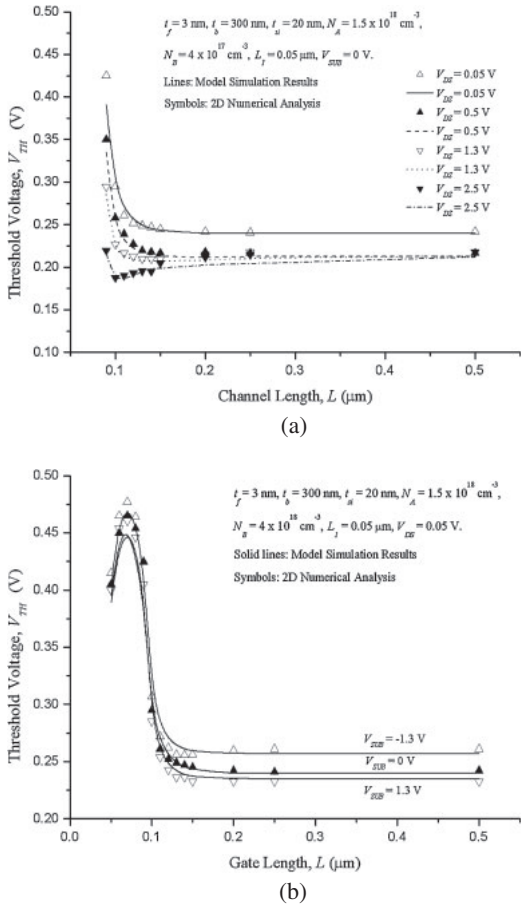

Fig. 4. Plot of the threshold voltage V_{TH} vs the gate length L for FD halo-implanted SOI MOSFETs with different bias voltages. (a) Drain–source voltages V_{DS} and (b) substrate bias voltage V_{SUB}.

structure with uniformly doped channel, halo, and drain/source regions, as shown in Fig. 1. In this subsection, only the case of $2L_1 < L$ is considered and we have presented some numerical results to demonstrate the DIBL effects on the subthreshold surface potential and threshold voltage of the short-channel SOI MOS transistors with halo implants and DIBL effects on the subthreshold current variation considering a wide range of parameters of the devices.

In Fig. 3, the variation in the front surface potential $\Psi_{fs}(x)$ as a function of the normalized position x/L along the channel length has been shown for different gate lengths and drain bias voltages. From the figure, it is observed that, for a fixed channel length, as the drain–source voltage V_{DS} is increased, the surface potential near the drain side increases which may result in a considerable reduction in the channel barrier height. The channel barrier is defined as the potential difference between the minimum surface potential and the source side potential. Furthermore, it is observed that for a fixed V_{DS}, the surface potential located near the drain side also increases with decreasing L. Although the surface potential near the drain side increases with the increase in V_{DS} as well as with the decrease in L, the minimum surface potential near the source side and the location of the minimum surface potential remain almost unchanged, especially for small drain voltages and large channel lengths. The insensitivity of the minimum surface potential to the drain bias voltage results from the fact that the enhanced electric encroachment from the drain region to the channel region as V_{DS} increases is absorbed by the depletion charge in the halo region near the drain side ($L_2 < x < L$), which has a high doping concentration N_A. Therefore, the DIBL effect is improved and the roll-off of the threshold voltage in short-channel devices may be retarded. Figure 4 shows the effects of the drain–source V_{DS} and the substrate bias V_{SUB} on the threshold voltage V_{TH} as a function of the channel length L. In Fig. 4(a), it is observed that, although the threshold voltage of the device may be shifted to a lower value as V_{DS} increases, the phenomenon of the sharp threshold voltage roll-off in the conventional MOSFET without halo implants is improved. The sharp roll-up of the threshold voltage in the figure exists owing to the high doping concentration in the halo region. With the appropriate design of the doping concentrations in the halo and channel regions, a smooth variation in the threshold voltage may be obtained. In Fig. 4(b), it is seen that, for the long-channel halo devices ($L > 2L_1$), a more negative substrate voltage biased results in an increase in the threshold voltage. However, for the short-channel halo devices ($L < 2L_1$), the effect of the substrate bias V_{SUB} on the threshold voltage is smaller owing to the high doping concentration in the channel region. Therefore, it may be observed that biasing at a negative substrate voltage may be a better choice to minimize the DIBL effect, which

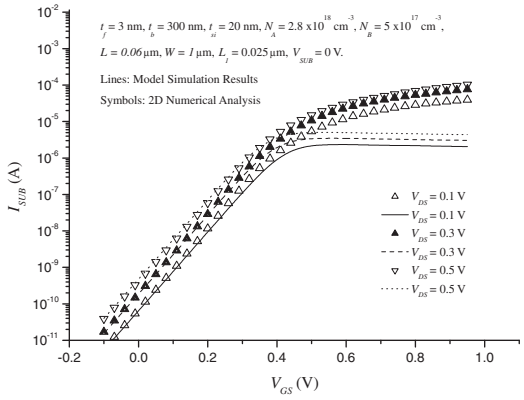

Fig. 5. Plot of the subthreshold current I_{SUB} vs the gate–source voltage V_{GS} for FD halo-implanted SOI MOSFETs of $L = 0.06\,\mu m$ with different drain–source voltages V_{DS}.

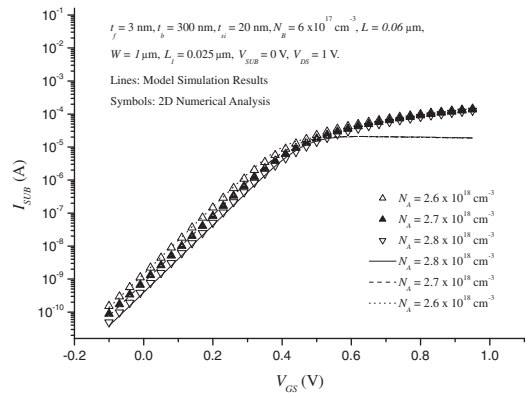

Fig. 7. Plot of the subthreshold current I_{SUB} vs the gate–source voltage V_{GS} for FD halo-implanted SOI MOSFETs of $L = 0.06\,\mu m$ with different halo doping concentrations N_A.

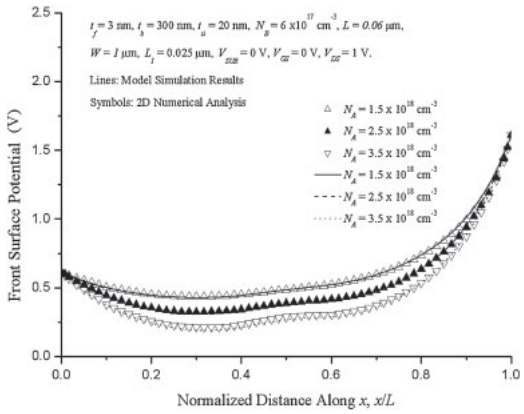

Fig. 6. Plot of the front surface potential $\Psi_{fs}(x)$ as a function of the normalized position (x/L) along the channel length for FD halo-implanted SOI MOSFETs of $L = 0.06\,\mu m$ with different halo doping concentrations N_A.

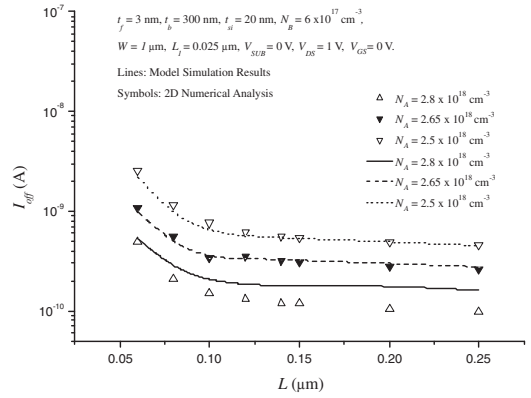

Fig. 8. Plot of the off-state current I_{off} vs the gate length L for FD halo-implanted SOI MOSFETs with different halo doping concentrations N_A.

may substantially improve the threshold voltage degradation. Figure 5 shows a plot of the subthreshold current I_{SUB} against the gate–source voltage V_{GS} with V_{DS} as the parameter. It is observed that, although the MOS transistor is with halo regions, the subthreshold current increases with the increase in V_{DS} owing to the enhanced electric encroachment from the drain region to the channel region and the small channel length. The calculated results have been compared with the results obtained using the Medici software, and good agreement is achieved for a gate length down to 0.06 μm, which shows the validity of the proposed analytical model.

Figure 6 shows a comparison of the surface potentials obtained using the present model and Medici as a function of the normalized position along the channel with the halo doping concentration N_A as the parameter. It is observed that, at a fixed V_{GS}, the surface potential of the halo MOS device with a higher halo doping concentration is shifted to a lower level, resulting in an increase in the channel barrier height. The effect of the halo doping concentration on the subthreshold current is shown in the plot of I_{SUB} vs V_{GS} in Fig. 7. It is seen that the subthreshold current of the MOSFET with a higher halo doping concentration is lower due to the increased barrier height. Figure 8 shows the off-state current I_{off} against the channel length L with the halo doping concentration N_A as the parameter, where $I_{off} = I_{SUB}$ at $V_{GS} = 0\,V$. It is seen that at a fixed N_A, I_{off} increases with the decrease in L owing to the short-channel effect. Furthermore, it is observed that, for a fixed channel length L, I_{off} decreases with the increase in N_A owing to the lower minimum surface potential and higher channel barrier height.

Figure 9 shows the effect of the channel doping concentration N_B on the surface potential as a function of the normalized position (x/L) along the channel length. It is seen that the location of the minimum surface potential remains almost the same and only a small variation in the surface potential is observed in the channel region $(L_1 < x < L_2)$ as N_B varies owing to the high doping concentration in the halo regions. Owing to the high halo doping concentration, the effect of the channel doping concentration N_B on the subthreshold current I_{SUB} is very small and is shown in Fig. 10. In this figure, only a small increase in subthreshold current is observed as N_B increases from 5×10^{17} to $7 \times 10^{17}\,cm^{-3}$.

The surface potential profiles $\Psi_{fs}(x)$ as a function of the normalized position (x/L) along the channel length for the halo MOSFETs of $L = 0.09\,\mu m$ with the length of the halo region, L_1, as the parameter is shown in Fig. 11. From the figure, it is seen that the position of the minimum surface potential, located in the source side halo region shifts toward the source side as the length of the halo region is reduced.

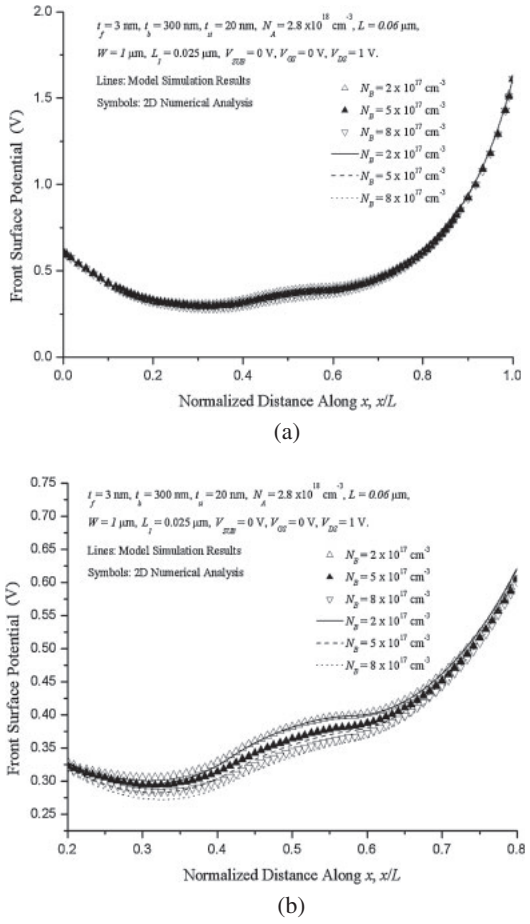

Fig. 9. (a) Plot of the front surface potential $\Psi_{fs}(x)$ as a function of the normalized position (x/L) along the channel length for FD halo-implanted SOI MOSFETs of $L = 0.06\,\mu m$ with different channel doping concentrations N_B. (b) Enlarged part of (a).

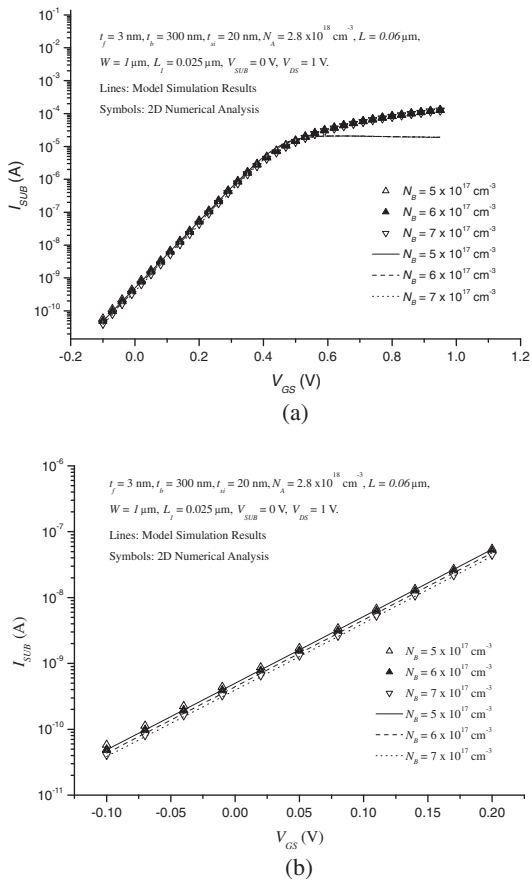

Fig. 10. Plot of the subthreshold current I_{SUB} vs the gate–source voltage V_{GS} for FD halo-implanted SOI MOSFETs of $L = 0.06\,\mu m$ with different channel doping concentrations N_B.

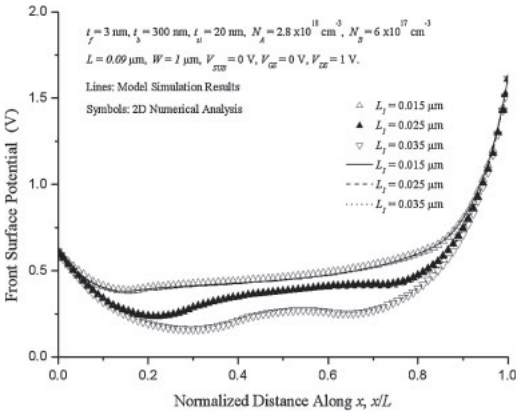

Fig. 11. Surface potential profiles $\Psi_{fs}(x)$ as a function of the normalized position (x/L) along the channel length for FD halo-implanted SOI MOSFETs of $L = 0.09\,\mu m$ with the length of the halo region L_1 as the parameter.

Moreover, it is observed that the surface potential minima in the three cases are not the same. The minimum surface potential shifts to a higher value as the length of the halo region is reduced. This occurs because the average doping concentration in the silicon film controlled by the gate increases as the length of the halo region, L_1, is increased. For a fixed channel length and a halo doping profile, as the length of the halo region decreases from 0.035 to 0.015 μm, the off-state current I_{off} increases from 1.84 pA/μm to 59.6 nA/μm, obtained from 2D numerical analysis. The above results have been compared with the numerical analysis obtained using the 2D device simulator Medici, and satisfactory agreement is obtained.

4. Conclusions

In this paper, new analytical models of the subthreshold surface potential, threshold voltage and subthreshold current of fully depleted SOI MOSFETs with halo or pocket implants have been proposed. Analytical and closed-form expressions have been obtained for both the front surface potential and the threshold voltage by solving Poisson's equation with the appropriate boundary conditions. Then, together with the conventional drift-diffusion current theory, an analytical subthreshold current model is also presented for halo-implanted SOI MOSFET devices. The results obtained using the model have been compared with those obtained using the 2D numerical device simulator Medici considering a wide range of structure parameters. Good agreement is achieved between the results of the model calculation and numerical analysis. To the best of our knowledge, these are first 2D models of FD SOI MOSFETs with halo or pocket implants, considering the subthreshold surface potential, threshold voltage, and subthreshold current at the same time.

Appendix A: Coefficients of second-order nonhomogenous differential equations

The expressions of the coefficients A_i, B_i, C_i, F_i, G_i, and H_i in Eq. (12) are given as follows.

$$A_1 = A_2 = A_3 = (-1)\left(\frac{2}{t_{si}^2}\right)\left(3 + \frac{2C_f}{C_{si}}\right), \quad B_1 = B_2 = B_3 = \left(\frac{2}{t_{si}^2}\right)\left(3 + \frac{C_b}{C_{si}}\right),$$
$$F_1 = F_2 = F_3 = \left(\frac{2}{t_{si}^2}\right)\left(3 + \frac{C_f}{C_{si}}\right), \quad G_1 = G_2 = G_3 = (-1)\left(\frac{2}{t_{si}^2}\right)\left(3 + \frac{2C_b}{C_{si}}\right),$$
$$C_1 = C_3 = \frac{qN_A}{\varepsilon_{si}} + \frac{2}{t_{si}^2}\left(\frac{C_b V'_{SUB,1} - 2C_f V'_{GS,1}}{C_{si}}\right), \quad H_1 = H_3 = \frac{qN_A}{\varepsilon_{si}} - \frac{2}{t_{si}^2}\left(\frac{2C_b V'_{SUB,1} - C_f V'_{GS,1}}{C_{si}}\right),$$
$$C_2 = \frac{qN_B}{\varepsilon_{si}} + \frac{2}{t_{si}^2}\left(\frac{C_b V'_{SUB,2} - 2C_f V'_{GS,2}}{C_{si}}\right), \quad H_2 = \frac{qN_B}{\varepsilon_{si}} - \frac{2}{t_{si}^2}\left(\frac{2C_b V'_{SUB,1} - C_f V'_{GS,1}}{C_{si}}\right). \tag{A·1}$$

Appendix B: Particular solutions $\Psi_{fsp,i}(x)$ and $\Psi_{bsp,i}(x)$, and the constants g_1, g_2, d_1, and d_2 of the general solution

The expressions of the particular solutions $\Psi_{fsp,i}(x)$ and $\Psi_{bsp,i}(x)$, and the constants g_1, g_2, d_1, and d_2 are given as follows.

$$\Psi_{fsp,1} = \lambda_1 \cdot V_{GS} + \lambda_2 \cdot V_{SUB} + \lambda_3 = \Psi_{fsp,3}, \quad \Psi_{fsp,2} = \lambda_1 \cdot V_{GS} + \lambda_2 \cdot V_{SUB} + \lambda_4,$$
$$\Psi_{bsp,1} = \lambda_5 \cdot V_{SUB} + \lambda_6 \cdot V_{GS} + \lambda_7 = \Psi_{bsp,3}, \quad \Psi_{bsp,2} = \lambda_5 \cdot V_{SUB} + \lambda_6 \cdot V_{GS} + \lambda_8$$
$$\lambda_1 = C_T \cdot \left(\frac{1}{C_b} + \frac{1}{C_{si}}\right),$$
$$\lambda_2 = \frac{C_T}{C_f},$$
$$\lambda_3 = \frac{C_T}{C_f} \cdot \left(\frac{1}{C_b} + \frac{1}{2C_{si}}\right) \cdot (-qN_A t_{si}) - \lambda_1 \cdot (V_{fbf,1} + \Psi_{FP,1}) - \lambda_2 \cdot (V_{fbb,1} + \Psi_{FP,1}),$$
$$\lambda_4 = \frac{C_T}{C_f} \cdot \left(\frac{1}{C_b} + \frac{1}{2C_{si}}\right) \cdot (-qN_B t_{si}) - \lambda_1 \cdot (V_{fbf,2} + \Psi_{FP,2}) - \lambda_2 \cdot (V_{fbb,2} + \Psi_{FP,2}),$$
$$\lambda_5 = C_T \cdot \left(\frac{1}{C_f} + \frac{1}{C_{si}}\right),$$
$$\lambda_6 = \frac{C_T}{C_b},$$
$$\lambda_7 = \frac{C_T}{C_b} \cdot \left(\frac{1}{C_f} + \frac{1}{2C_{si}}\right) \cdot (-qN_A t_{si}) - \lambda_5 \cdot (V_{fbb,1} + \Psi_{FP,1}) - \lambda_6 \cdot (V_{fbf,1} + \Psi_{FP,1}),$$
$$\lambda_8 = \frac{C_T}{C_b} \cdot \left(\frac{1}{C_b} + \frac{1}{2C_{si}}\right) \cdot (-qN_B t_{si}) - \lambda_5 \cdot (V_{fbb,2} + \Psi_{FP,2}) - \lambda_6 \cdot (V_{fbf,2} + \Psi_{FP,2}),$$
$$\lambda_9 = d_2 \cdot \{(g_1 - 1) \cdot V_{bi} + [g_1(\lambda_7 - \lambda_8) + (\lambda_4 - \lambda_3)] \cdot \cosh(d_2 L_1) + (\lambda_3 - g_1\lambda_7)\},$$
$$\lambda_{10} = d_1 \cdot \{(g_2 - 1) \cdot V_{bi} + [g_2(\lambda_7 - \lambda_8) + (\lambda_4 - \lambda_3)] \cdot \cosh(d_1 L_1) + (\lambda_3 - g_2\lambda_7)\},$$
$$\lambda_{11} = d_2 \cdot \{-(g_1 - 1) \cdot (V_{bi} + V_{DS}) + [g_1(\lambda_8 - \lambda_7) + (\lambda_3 - \lambda_4)] \cdot \cosh(d_2(L_2 - L)) + (g_1\lambda_7 - \lambda_3)\},$$
$$\lambda_{12} = d_1 \cdot \{-(g_2 - 1) \cdot (V_{bi} + V_{DS}) + [g_2(\lambda_8 - \lambda_7) + (\lambda_3 - \lambda_4)] \cdot \cosh(d_1(L_2 - L)) + (g_2\lambda_7 - \lambda_3)\}. \tag{B·1}$$

$$g_1 = (-1)\frac{\frac{\varepsilon_{ox}}{\varepsilon_{si}}\left(\frac{1}{t_f} - \frac{1}{t_b}\right) + \sqrt{\left(\frac{\varepsilon_{ox}}{\varepsilon_{si}}\right)^2\left(\frac{1}{t_f} - \frac{1}{t_b}\right)^2 + \left(\frac{\varepsilon_{ox}}{\varepsilon_{si}}\right)^2 \frac{1}{t_f t_b} + \frac{9}{t_{si}^2} + \frac{\varepsilon_{ox}}{\varepsilon_{si}} \cdot \frac{3}{t_{si}}\left(\frac{1}{t_f} + \frac{1}{t_b}\right)}}{\frac{3}{t_{si}} + \frac{C_f}{\varepsilon_{si}}}$$

$$g_2 = (-1)\frac{\frac{\varepsilon_{ox}}{\varepsilon_{si}}\left(\frac{1}{t_f} - \frac{1}{t_b}\right) - \sqrt{\left(\frac{\varepsilon_{ox}}{\varepsilon_{si}}\right)^2\left(\frac{1}{t_f} - \frac{1}{t_b}\right)^2 + \left(\frac{\varepsilon_{ox}}{\varepsilon_{si}}\right)^2 \frac{1}{t_f t_b} + \frac{9}{t_{si}^2} + \frac{\varepsilon_{ox}}{\varepsilon_{si}} \cdot \frac{3}{t_{si}}\left(\frac{1}{t_f} + \frac{1}{t_b}\right)}}{\frac{3}{t_{si}} + \frac{C_f}{\varepsilon_{si}}}$$

$$d_1 = \left[\frac{6}{t_{si}^2} + \frac{\varepsilon_{ox}}{\varepsilon_{si}} \cdot \frac{2}{t_{si}}\left(\frac{1}{t_f} + \frac{1}{t_b}\right) + \frac{2}{t_{si}}\sqrt{\left(\frac{\varepsilon_{ox}}{\varepsilon_{si}}\right)^2\left(\frac{1}{t_f} - \frac{1}{t_b}\right)^2 + \left(\frac{\varepsilon_{ox}}{\varepsilon_{si}}\right)^2 \frac{1}{t_f t_b} + \frac{9}{t_{si}^2} + \frac{\varepsilon_{ox}}{\varepsilon_{si}} \cdot \frac{3}{t_{si}}\left(\frac{1}{t_f} + \frac{1}{t_b}\right)}\right]^{1/2}$$

$$d_2 = \left[\frac{6}{t_{si}^2} + \frac{\varepsilon_{ox}}{\varepsilon_{si}} \cdot \frac{2}{t_{si}}\left(\frac{1}{t_f} + \frac{1}{t_b}\right) - \frac{2}{t_{si}}\sqrt{\left(\frac{\varepsilon_{ox}}{\varepsilon_{si}}\right)^2\left(\frac{1}{t_f} - \frac{1}{t_b}\right)^2 + \left(\frac{\varepsilon_{ox}}{\varepsilon_{si}}\right)^2 \frac{1}{t_f t_b} + \frac{9}{t_{si}^2} + \frac{\varepsilon_{ox}}{\varepsilon_{si}} \cdot \frac{3}{t_{si}}\left(\frac{1}{t_f} + \frac{1}{t_b}\right)}\right]^{1/2} \tag{B·2}$$

Appendix C: Coefficients of the analytical solution of the surface potential

The expressions of the coefficients a_{i1}, a_{i2}, a_{i3}, and a_{i4} of the solution of the subthreshold surface potential in region i are given as follows.

$$a_{11} = \alpha_1 \cdot V_{GS} + \alpha_2 \cdot V_{SUB} + \alpha_3, \quad a_{12} = \alpha_4 \cdot V_{GS} + \alpha_5 \cdot V_{SUB} + \alpha_6,$$
$$a_{13} = \alpha_7 \cdot V_{GS} + \alpha_8 \cdot V_{SUB} + \alpha_9, \quad a_{14} = \alpha_{10} \cdot V_{GS} + \alpha_{11} \cdot V_{SUB} + \alpha_{12}$$

$$\alpha_1 = \frac{(g_2\lambda_6 - \lambda_1)\cdot(e^{-d_1 L} - 1)}{2\cdot(g_2 - g_1)\cdot\sinh(d_1 L)}, \quad \alpha_2 = \frac{(g_2\lambda_5 - \lambda_2)\cdot(e^{-d_1 L} - 1)}{2\cdot(g_2 - g_1)\cdot\sinh(d_1 L)},$$

$$\alpha_3 = \frac{1}{2(g_2 - g_1)\cdot\sinh(d_1 L_1)}\cdot\left\{e^{-d_1 L_1}\cdot[g_2\lambda_7 - \lambda_3 - (g_2 - 1)\cdot V_{bi}] + g_2(\lambda_8 - \lambda_7) + (\lambda_3 - \lambda_4)\right.$$
$$\left. + (-1)\cdot\frac{[\lambda_{10}\cdot\sinh(d_1\cdot(L_1 - L)) + \lambda_{12}\cdot\sinh(d_1 L_1)]}{d_1\sinh(d_1 L)}\right\},$$

$$\alpha_4 = \frac{(\lambda_1 - g_2\lambda_6)\cdot(e^{d_1 L} - 1)}{2\cdot(g_2 - g_1)\cdot\sinh(d_1 L)}, \quad \alpha_5 = \frac{(\lambda_2 - g_2\lambda_5)\cdot(e^{d_1 L} - 1)}{2\cdot(g_2 - g_1)\cdot\sinh(d_1 L)},$$

$$\alpha_6 = \frac{(-1)}{2(g_2 - g_1)\cdot\sinh(d_1 L_1)}\cdot\left\{e^{d_1 L_1}\cdot[g_2\lambda_7 - \lambda_3 - (g_2 - 1)\cdot V_{bi}] + g_2(\lambda_8 - \lambda_7) + (\lambda_3 - \lambda_4)\right.$$
$$\left. + (-1)\cdot\frac{[\lambda_{10}\cdot\sinh(d_1\cdot(L_1 - L)) + \lambda_{12}\cdot\sinh(d_1 L_1)]}{d_1\sinh(d_1 L)}\right\},$$

$$\alpha_7 = \frac{(g_1\lambda_6 - \lambda_1)\cdot(e^{-d_2 L} - 1)}{2\cdot(g_1 - g_2)\cdot\sinh(d_2 L)}, \quad \alpha_8 = \frac{(g_1\lambda_5 - \lambda_2)\cdot(e^{-d_2 L} - 1)}{2\cdot(g_1 - g_2)\cdot\sinh(d_2 L)},$$

$$\alpha_9 = \frac{1}{2(g_1 - g_2)\cdot\sinh(d_2 L_1)}\cdot\left\{e^{-d_2 L_1}\cdot[g_1\lambda_7 - \lambda_3 - (g_1 - 1)\cdot V_{bi}] + g_1(\lambda_8 - \lambda_7) + (\lambda_3 - \lambda_4)\right.$$
$$\left. + (-1)\cdot\frac{[\lambda_9\cdot\sinh(d_2\cdot(L_1 - L)) + \lambda_{11}\cdot\sinh(d_2 L_1)]}{d_2\sinh(d_2 L)}\right\},$$

$$\alpha_{10} = \frac{(\lambda_1 - g_1\lambda_6)\cdot(e^{d_2 L} - 1)}{2\cdot(g_1 - g_2)\cdot\sinh(d_2 L)}, \quad \alpha_{11} = \frac{(\lambda_2 - g_1\lambda_5)\cdot(e^{d_2 L} - 1)}{2\cdot(g_1 - g_2)\cdot\sinh(d_2 L)},$$

$$\alpha_{12} = \frac{(-1)}{2(g_1 - g_2)\cdot\sinh(d_2 L_1)}\cdot\left\{e^{d_2 L_1}\cdot[g_1\lambda_7 - \lambda_3 - (g_1 - 1)\cdot V_{bi}] + g_1(\lambda_8 - \lambda_7) + (\lambda_3 - \lambda_4)\right.$$
$$\left. + (-1)\cdot\frac{[\lambda_9\cdot\sinh(d_2\cdot(L_1 - L)) + \lambda_{11}\cdot\sinh(d_2 L_1)]}{d_2\sinh(d_2 L)}\right\},$$

$$a_{21} = \delta_1 \cdot V_{GS} + \delta_2 \cdot V_{SUB} + \delta_3, \quad a_{22} = \delta_4 \cdot V_{GS} + \delta_5 \cdot V_{SUB} + \delta_6,$$
$$a_{23} = \delta_7 \cdot V_{GS} + \delta_8 \cdot V_{SUB} + \delta_9, \quad a_{24} = \delta_{10} \cdot V_{GS} + \delta_{11} \cdot V_{SUB} + \delta_{12},$$

$$\delta_1 = \frac{(g_2\lambda_6 - \lambda_1)\cdot(1 - e^{-d_1 L})}{2(g_1 - g_2)\cdot\sinh(d_1 L)}, \quad \delta_2 = \frac{(g_2\lambda_5 - \lambda_2)\cdot(1 - e^{-d_1 L})}{2(g_1 - g_2)\cdot\sinh(d_1 L)}, \quad \delta_3 = \frac{\lambda_{12} + \lambda_{10}\cdot e^{-d_1 L}}{2d_1(g_1 - g_2)\cdot\sinh(d_1 L)},$$

$$\delta_4 = -\frac{(g_2\lambda_6 - \lambda_1)\cdot(1 - e^{d_1 L})}{2(g_1 - g_2)\cdot\sinh(d_1 L)}, \quad \delta_5 = -\frac{(g_2\lambda_5 - \lambda_2)\cdot(1 - e^{d_1 L})}{2(g_1 - g_2)\cdot\sinh(d_1 L)}, \quad \delta_6 = \frac{\lambda_{12} + \lambda_{10}\cdot e^{d_1 L}}{2d_1(g_1 - g_2)\cdot\sinh(d_1 L)},$$

$$\delta_7 = \frac{(g_1\lambda_6 - \lambda_1)\cdot(1 - e^{-d_2 L})}{2(g_2 - g_1)\cdot\sinh(d_2 L)}, \quad \delta_8 = \frac{(g_1\lambda_5 - \lambda_2)\cdot(1 - e^{-d_2 L})}{2(g_2 - g_1)\cdot\sinh(d_2 L)}, \quad \delta_9 = \frac{\lambda_{11} + \lambda_9\cdot e^{-d_2 L}}{2d_2(g_2 - g_1)\cdot\sinh(d_2 L)},$$

$$\delta_{10} = -\frac{(g_1\lambda_6 - \lambda_1)\cdot(1 - e^{d_2 L})}{2(g_2 - g_1)\cdot\sinh(d_2 L)}, \quad \delta_{11} = -\frac{(g_1\lambda_5 - \lambda_2)\cdot(1 - e^{d_2 L})}{2(g_2 - g_1)\cdot\sinh(d_2 L)}, \quad \delta_{12} = \frac{\lambda_{11} + \lambda_9\cdot e^{d_2 L}}{2d_2(g_2 - g_1)\cdot\sinh(d_2 L)}$$

$$a_{31} = \frac{1}{(g_2 - g_1)\cdot(e^{d_1(L_2 - 2L)} - e^{-d_1 L_2})}\cdot\{(-1)\cdot[(g_2 - 1)(V_{bi} + V_{DS}) - g_2\Psi_{bsp,3} + \Psi_{fsp,2}]\cdot e^{-d_1(L_2 + L)}$$
$$+ (g_2 - g_1)\cdot e^{-2d_1 L}(b_1 e^{d_1 L_2} + b_2 e^{-d_1 L_2}) + [g_2(\lambda_8 - \lambda_7) + (\lambda_3 - \lambda_4)]\cdot e^{-2d_1 L}\}$$

$$a_{32} = \frac{1}{(g_2 - g_1)\cdot(e^{d_1(L_2 - 2L)} - e^{-d_1 L_2})}\cdot\{[(g_2 - 1)(V_{bi} + V_{DS}) - g_2\Psi_{bsp,3} + \Psi_{fsp,2}]\cdot e^{d_1(L_2 - L)}$$
$$- (g_2 - g_1)\cdot(b_1 e^{d_1 L_2} + b_2 e^{-d_1 L_2}) + [g_2(\lambda_7 - \lambda_8) + (\lambda_4 - \lambda_3)]\}$$

$$a_{33} = \frac{1}{(g_1 - g_2)\cdot(e^{d_2(L_2 - 2L)} - e^{-d_2 L_2})}\cdot\{(-1)\cdot[(g_1 - 1)(V_{bi} + V_{DS}) - g_1\Psi_{bsp,3} + \Psi_{fsp,2}]\cdot e^{-d_2(L_2 + L)}$$
$$+ (g_1 - g_2)\cdot e^{-2d_2 L}(b_3 e^{d_2 L_2} + b_4 e^{-d_2 L_2}) + [g_1(\lambda_8 - \lambda_7) + (\lambda_3 - \lambda_4)]\cdot e^{-2d_2 L}\}$$

$$a_{34} = \frac{1}{(g_1 - g_2)\cdot(e^{d_2(L_2-2L)} - e^{-d_2L_2})} \cdot \{[(g_1 - 1)(V_{bi} + V_{DS}) - g_1\Psi_{bsp,3} + \Psi_{fsp,2}] \cdot e^{d_2(L_2-L)} - (g_1 - g_2)\cdot(b_3 e^{d_2L_2} + b_4 e^{-d_2L_2}) + [g_1(\lambda_7 - \lambda_8) + (\lambda_4 - \lambda_3)]\}. \quad (C{\cdot}1)$$

1) V. P. Trivedi and J. G. Fossum, IEEE Trans. Electron Devices **50**, 2095 (2003).
2) S. T. Liu, W. C. Jenkins, and H. L. Hughes, IEEE Trans. Nucl. Sci. **45**, 2442 (1998).
3) J.-P. Colinge, *Silicon-on-Insulator Technology: Materials to VLSI* (Kluwer Academic, Boston, MA, 1991) Chap. 1.
4) L. Geppert, IEEE Spectrum **36**, 52 (1999).
5) B. Yu, C. H. Wanna, E. D. Nowak, K. Noda, and C. Hu, IEEE Trans. Electron Devices **44**, 627 (1997).
6) B. Yu, H. Wang, O. Milic, Q. Xiang, W. Wang, J. X. An, and M.-R. Lin, IEDM Tech. Dig., 1999, p. 653.
7) Y. Taur, D. A. Buchanan, W. Chen, D. J. Frank, K. E. Ismail, S.-H. Lin, G. A. Saihalasz, R. G. Viswanathan, H. C. Wanna, S. J. Wind, and H. S. Wong, Proc. IEEE **85**, 486 (1997).
8) K. M. Cao, W. Liu, X. Jin, K. Vashanth, K. Green, J. Krick, T. Vrotsos, and C. Hu, IEDM Tech. Dig., 1999, p. 171.
9) A. Chatterjee, K. Vasanth, D. T. Grider, M. Nandakumar, G. Pollack, R. Aggarwal, M. Rodder, and H. Shichijo, Symp. VLSI Technology Dig. Tech. Pap., 1999, p. 147.
10) M. Dehan and J. P. Raskin, Solid-State Electron. **46**, 1005 (2002).
11) J. Hoentschel, A. Wei, M. Wiatr, A. Gehring, T. Scheiper, R. Mulfinger, T. Feudel, T. Lingner, A. Poock, S. Muehle, C. Krueger, T. Herrmann, W. Klix, R. Stenzel, R. Stephan, P. Huebler, T. Kammler, P. Shi, M. Raab, D. Greenlaw, and M. Horstmann, IEDM Tech. Dig., 2008, p. 649.
12) N. Hakim, V. R. Rao, J. Vasi, and J. C. S. Woo, IEEE Trans. Device Mater. Reliab. **5**, 127 (2005).
13) D. G. Borse, K. N. Manjula Rani, N. K. Jha, A. N. Chandorkar, J. Vasi, V. Ramgopal Rao, B. Cheng, and J. C. S. Woo, IEEE Trans. Electron Devices **49**, 1077 (2002).
14) R. S. Santiesteban, G. C. Abeln, T. E. Beatty, and O. Rodriguez, IEEE Trans. Semicond. Manuf. **16**, 653 (2003).
15) S. Chakraborty, A. Mallik, C. K. Sarkar, and V. R. Rao, IEEE Trans. Electron Devices **54**, 241 (2007).
16) MEDICI ver4.0 (1998).
17) R. Zhang and K. Roy, IEEE Trans. Electron Devices **49**, 852 (2002).
18) J. C. S. Woo, K. W. Terrill, and P. K. Vasudev, IEEE Trans. Electron Devices **37**, 1999 (1990).
19) T. C. Hsiao and J. C. S. Woo, IEEE Trans. Electron Devices **42**, 1120 (1995).
20) S. Veeraraghavan and J. G. Fossum, IEEE Trans. Electron Devices **36**, 522 (1989).
21) K. K. Young, IEEE Trans. Electron Devices **36**, 399 (1989).
22) G. Zhang, Z. Shao, and K. Zhou, IEEE Trans. Electron Devices **55**, 803 (2008).
23) G. Zhang, K. Chen, X. Zheng, F. Liang, and Z. Li, Jpn. J. Appl. Phys. **52**, 014301 (2013).
24) N. Sadachika, D. Kitamaru, Y. Uetsuji, D. Navarro, M. M. Yusoff, T. Ezaki, H. J. Mattausch, and M. M. Mattausch, IEEE Trans. Electron Devices **53**, 2017 (2006).
25) J. Y. Guo and C. Y. Wu, IEEE Trans. Electron Devices **40**, 1653 (1993).
26) R. Sharma, S. Pandey, and S. Bala Jain, Int. J. Numer. Modeling: Electron. Networks Devices Fields **27**, 173 (2014).
27) P. Pandey, B. B. Pal, and S. Jit, IEEE Trans. Electron Devices **51**, 246 (2004).
28) R. Rao, G. Katti, D. S. Havaldar, N. DasGupta, and A. DasGupta, Solid-State Electron. **53**, 256 (2009).
29) H. van Meer and K. D. Meyer, IEEE Trans. Electron Devices **48**, 2292 (2001).
30) P. C. Yeh and J. G. Fossum, IEEE Trans. Electron Devices **42**, 1605 (1995).
31) S. Biesemens and K. D. Meyer, Ext. Abstr. Int. Conf. Solid State Devices and Materials, 1994, p. 892.
32) S. Pidin and M. Koyanagi, Jpn. J. Appl. Phys. **37**, 1264 (1998).
33) E. Kreyszig, *Advanced Engineering Mathematics* (Wiley, New York, 1983) 5th ed., p. 52.
34) T. A. Fjeldly and M. Shur, IEEE Trans. Electron Devices **40**, 137 (1993).
35) R. Gwoziecki, T. Skotnicki, P. Bouillon, and P. Gentil, IEEE Trans. Electron Devices **46**, 1551 (1999).